

## ARTICLE OPEN



# Interpass temperature effects on WAAM ER316L stainless steel corrosion using potentiostatic pulse tests

Corentin Penot<sup>1,2</sup>✉, Julian Wharton<sup>1</sup>, Adrian Addison<sup>3</sup>, Yikun Wang<sup>4</sup> and Qing Lu<sup>3</sup>

The effect of interpass temperature on the microstructure and pit nucleation behaviour in wire and arc additive manufacturing (WAAM) deposited ER316L stainless steel is investigated. Lowering the interpass temperature increases the ferrite content and decreases the sigma phase precipitation. Potentiostatic pulse measurements show that the WAAM ER316L pits develop predominantly near sigma phases and have higher pit density compared to a wrought 316L (UNS S31600). The pitting susceptibility of WAAM ER316L increases with increasing interpass temperature due to the precipitation of larger sigma phase enhancing the elemental segregation.

*npj Materials Degradation* (2023)7:89; <https://doi.org/10.1038/s41529-023-00408-8>

## INTRODUCTION

Additive Manufacturing (AM) has received increasing industrial interest in recent years as it has demonstrated promising advantages to shorten manufacture lead times, increase design freedom and reduce material wastage. Among various AM processes, the wire and arc additive manufacturing (WAAM) is a wire based direct energy deposition process featuring an arc welding torch as the deposition head that is attached to a multi-axis robot arm. WAAM can manufacture large metallic structures of several metres in size due to its open-air nature and high deposition rate (several  $\text{kg h}^{-1}$ )<sup>1–5</sup>. Various industry sectors such as maritime, oil and gas, nuclear and chemical processing are interested in pairing WAAM technologies with stainless steels such as 316 (UNS S31600)/316L (UNS S31603), since these sectors widely use 316L for large structural components for its inherent mechanical and corrosion performance. However, the rapid cooling gradients during welding and the thermal cycles during the AM deposition form complex non-equilibrium microstructures<sup>6–12</sup> which are dissimilar to the conventional wrought counterpart used for structural applications.

The study of corrosion behaviour of WAAM parts is scarce when compared to the vast number of studies on their mechanical properties. WAAM is a complex process with a wide range of parameters that often result in inconsistent corrosion results. For example, some studies have shown that the sigma ( $\sigma$ ) phase in WAAM-fabricated parts can decrease pitting resistance<sup>6,13,14</sup>. The presence of sigma phase reduces chromium levels in the matrix and lowers the pitting resistance. This was confirmed by polarization experiments in 3.5% NaCl solution and ASTM G48 immersion tests. Heat input has also been shown to affect the corrosion resistance, with high heat input resulting in lower pitting resistance<sup>14,15</sup>. Chromium and molybdenum segregation between the ferrite and austenite phase is thought to be the cause of the lower pitting resistance at high heat input. However, a study by Queguineur et al.<sup>16</sup> did not report the presence of sigma phase in WAAM deposited 316L (EN X2CrNiMo19-12) and found corrosion resistance comparable to a conventional laminated 316L (EN X2CrNiMo17-12-2). This highlights the need to further our

understanding in the effects of various parameters on WAAM component corrosion behaviour. Particularly, the influence of the interpass temperature on sigma precipitation and corrosion resistance has not been investigated and no definitive evidence of pit initiating at sigma phases was provided.

To date, potentiodynamic polarisation (PDP) is the preferred method to investigate the corrosion resistance of WAAM parts in the literature. However, it cannot provide detailed information on the pit nucleation sites. Recently, the Potentiostatic Pulse Technique (PPT) has been demonstrated to be a promising electrochemical technique to characterize the pitting behaviour of alloys with complex microstructures, such as laser AM deposited 316L<sup>17</sup> and microstructures containing sigma phase<sup>18</sup>. PPT was initially used to study hydrogen absorption in alloys<sup>19,20</sup> based on a series of cyclic potential steps (pulses). Subsequently, PPT was used by Chen et al.<sup>21</sup> to rapidly detect sensitization of austenitic stainless steel (ASS), and later was adapted by Kang and Frankel<sup>22</sup> to investigate early failure mechanisms of organic coatings. Gao et al.<sup>23</sup> use PPT to characterize pitting, where each potentiostatic pulse was divided into two phases: pit nucleation and the passivation phases. During the pit nucleation phase, the potential was maintained at a higher potential ( $E_h$ ) for a time step ( $t_h$ ), with  $E_h$  selected to be above the pitting potential ( $E_{\text{pit}}$ ) to initiate pits. Pits were passivated in the passivation phase by maintaining the potential at a lower potential ( $E_l$ ) for a time ( $t_l$ ), with  $E_l$  selected to be within the passivation domain. Gao et al. reported that the choice of appropriate parameters led to nucleation of small pits and allowed preferential pit nucleation sites to be identified in a duplex stainless steel (UNS S31803) using a combination of PPT and scanning electron microscopy (SEM) observations. Vignal et al.<sup>24</sup> combined PPT with optical microscopy (OM) and electron backscatter diffraction (EBSD) to study the pit size distribution in a low carbon martensitic stainless steel (X4CrNiMo16.5.1). Vignal et al. also used PPT to study the influence of inclusions on the pitting behaviour of an aged duplex stainless steel (UNS S32202)<sup>25</sup> and to study the corrosion resistance at different zones of a single pass weld 304L (UNS S30403) stainless steel specimens<sup>26</sup>. Interestingly, Sun et al.<sup>18</sup> used PPT to study sigma precipitation effects on the pitting resistance of a 317L alloy (UNS S31703) and

<sup>1</sup>National Centre for Advanced Tribology at Southampton (nCATS), Faculty of Engineering and Physical Sciences, University of Southampton, Southampton, UK. <sup>2</sup>The National Structural Integrity Research Centre (NSIRC), Granta Park, Cambridge, UK. <sup>3</sup>TWI Ltd, Granta Park, Cambridge, UK. <sup>4</sup>Lloyd's Register EMEA, Global Technology Centre, Hampshire House, Burgess Road, Hampshire Corporate Par, UK. ✉email: c.penot@soton.ac.uk

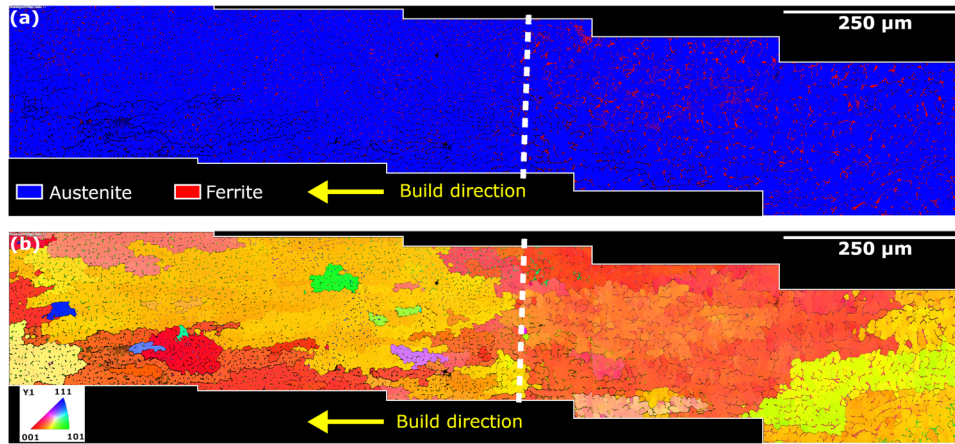


**Fig. 1** EBSD at a mid-height layer transition of WAAM ER316L stainless steel specimen from wall B2. **a** Phase and **b** crystallographic orientation map with respect to build direction ( $y$ ).

reported that the pitting resistance was related to the sigma content. Therefore, PPT appears as an effective method to investigate the pitting behaviour of complex microstructure, however, to date, it has not been implemented on WAAM deposited ER316L.

In this study we used PPT for the first time on WAAM fabricated ER316L parts, to investigate the effect of interpass temperature on the microstructure and sigma precipitation as well as its effect on pit nucleation. Two multilayer walls were fabricated with different interpass temperatures using a pulsed air cooling system. A PPT protocol was implemented to investigate the pit nucleation for the two WAAM ER316L walls as well as a wrought 316L.

## RESULTS

### Microstructure characterization

Figure 1 shows the EBSD phase and crystallographic orientation maps taken at mid-height of the interpass cooled wall (B2). The microstructure consists of an austenite matrix (blue) with delta ferrite (red) arranged in a semi-continuous network. The solidification structure was dendritic and the delta ferrite was located at the dendrite core region resulting in a reticular shape as can be seen in Fig. 1a. The dendrite growth direction was parallel to the build direction and the cooling gradient. A distinct layer transition is observed, as highlighted by the white dash line, where the secondary delta ferrite phase has an altered morphology. Dendrites were coarse on the right hand side of the line (the primary dendrite average spacing =  $10\ \mu\text{m}$ ) which corresponds to the top of the previous deposit layer and were refined on the left hand side of the line (the primary dendrite average spacing =  $6\ \mu\text{m}$ ) which corresponds to the remelting zone and the subsequent layer. The crystal lattice was mainly [001] oriented as shown in Fig. 1b. Large columnar grains were present and oriented parallel to the cooling gradient, following the dendrite growth direction, and a slight grain refinement occurred at the layer transition region.

Electroetching in 40% NaOH was performed to differentiate between the ferrite and sigma phases, i.e., sigma was over-etched compared to ferrite. Figure 2 shows the OM for the non-interpass cooled wall (B1) (a to d) and wall B2 (e to h) parallel and perpendicular to the build direction. Three phases are evident, the austenite matrix and delta ferrite phase, plus the sigma phase which was at the ferrite/austenite interface. The ferrite morphology was strongly related to the deposition, i.e., finer at the remelting zone and coarser at the top of the previous non-remelting layer. The overall solidification structures of B1 and B2

were comparable and akin to that described earlier in Fig. 1 (i.e., dendritic and oriented towards the build direction).

The average ferrite content was 4.3% in B1 and 6.4% in B2 (via Feritscope). SEM of the etched B1 and B2 vertical specimens provided a clearer distinction between ferrite and sigma phases (Fig. 3). Both B1 and B2 contained sigma (black) which clearly precipitated from the ferrite phase (dark grey). The sigma and ferrite contents in Fig. 3 were determined by evaluating the pixel count ratio of each phase: 4.7% and 7.1% ferrite, 0.9% and 0.1% sigma, for B1 and B2 specimens, respectively. The ferrite contents were generally in accordance with the Feritscope measurements. The sigma content was higher in B1 by approximately 0.8%. Sigma phases were larger in B1 covering a greater portion of the delta ferrite phase compared to B2 with largest phases  $>15\ \mu\text{m}$  in length in the former and  $<4\ \mu\text{m}$  in the latter, see Fig. 3. Additional, measurements were performed to determine the sigma content in B1 and B2 walls. The secondary phase content was determined from NaOH etched OM and compared with the ferrite content measured using a feritscope. The difference between the secondary phase and ferrite content was considered as the sigma phase. The detailed procedure is described in the Supplementary Methods. The estimated sigma content was found to be 1.1% and 0.2% in B1 and B2 walls, respectively, which supports the observations presented in Fig. 3.

### Potential step time optimisation

PPT was performed on specimens from B1 oriented horizontally ( $z, x$ ), namely B1-H1, B1-H2, B1-H3 and B1-H4 at four  $t_h$  durations: 0.5, 1, 2, and 4 s, respectively. Other key parameters including the  $T_{\text{sol}} = 40\ ^\circ\text{C}$ ,  $E_h = +450\ \text{mV}$ ,  $E_i = -160\ \text{mV}$ , and  $t_i = 5\ \text{s}$ , were selected to ensure:

- Pits nucleate within a short time span (typically less than a second) after  $E_h$  is applied.
- Pits passivate during the step time  $t_i$  where the potential is maintained at  $E_i$ .
- Pits grow to a detectable size using optical microscopy (typically greater than  $10\ \mu\text{m}^2$ ).

These parameters were chosen based on cyclic potentiodynamic polarization and critical pitting temperature tests. The selection rationale is described in the Supplementary Methods (see Supplementary Figs. 1 and 2, respectively). Prior to testing, the pre-PPT feature distribution was determined to assess the influence of non-corrosion related features on pit detection (see Supplementary Methods and Supplementary Fig. 3). The minimum pit size was set to be  $10\ \mu\text{m}^2$  to limit the influence of microstructure inclusions and polishing artifacts on pit detection.

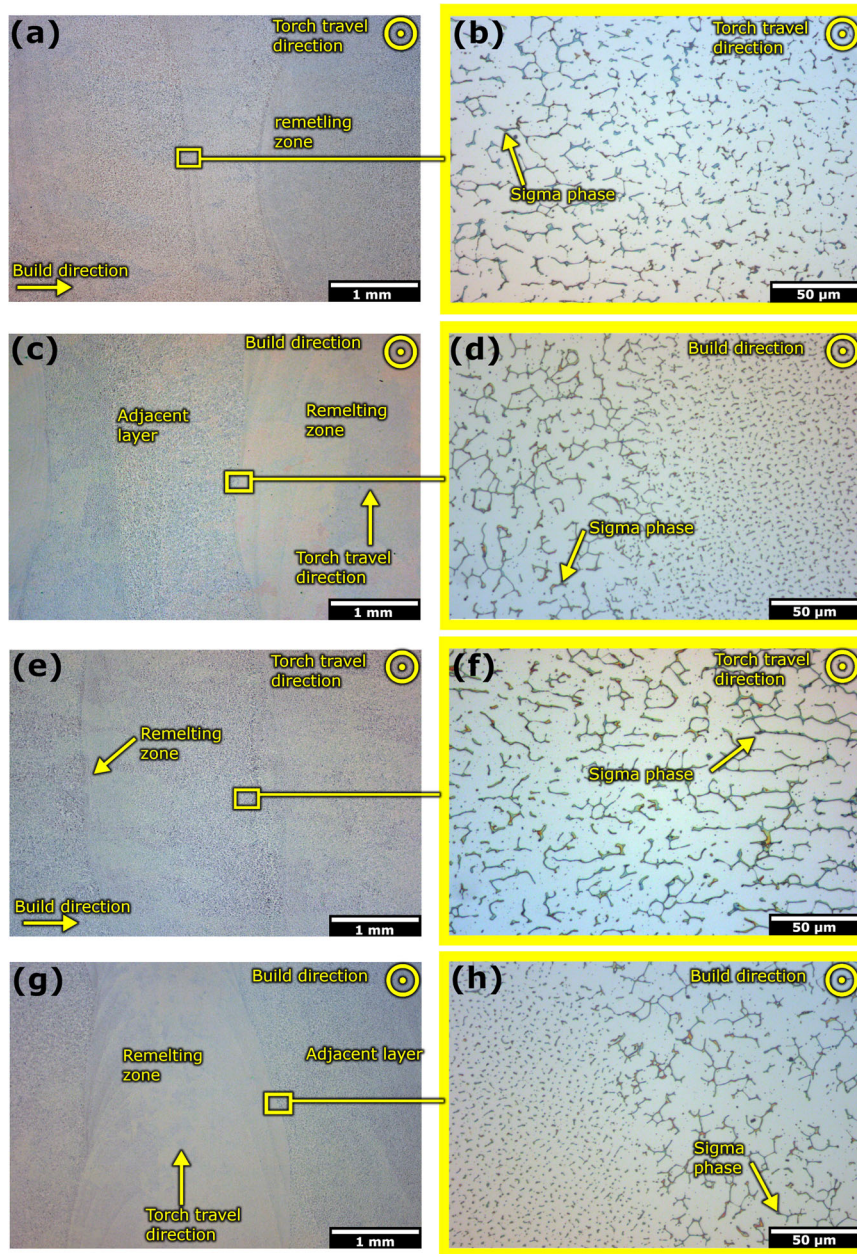


**Fig. 2** Optical microscopy of WAAM stainless steel ER316L after electro-etching in 40% NaOH. **a, b** B1 ( $x, y$ ) plane; **c, d** B1 ( $z, x$ ) plane; **e, f** B2 ( $x, y$ ) plane; and **g, h** B2 ( $z, x$ ) plane. Approximately 45 mm from the wall top.

Figure 4 shows the current density profiles during PPT for the four  $t_h$  durations. As expected, the current density transients (pulses) increased sharply during each high potential dwell time, associated with surface depassivation, i.e., pitting. The current density returns to the long-term baseline when the potential is held at  $E_h$ , indicating the nucleated pits repassivate. In all cases, the pulse amplitude ( $j_n$  where  $n$  is the pulse number) tended to increase achieving a maximum  $j_{max}$ , after which the subsequent pulse amplitudes gradually decrease until no activity was triggered by the potential step, at which point the test surface reaches a passive state ( $j_n < 0.1 \text{ mA cm}^{-2}$ ). Note at this point non-faradaic processes such as surface charging/discharging effects provide the passive current. To quantify the number of pulses to reach the final passive surface state, the  $n_{98\%}$  parameter was defined as the pulse number at 98% of the total charge density ( $Q_{tot}$ ).  $Q_{tot}$  was obtained by integrating the current density over

the entire test duration. Other useful indicators were evaluated from the current density profiles (see Table 1 for each  $t_h$ ):

- The mean current density ( $j_{mean}$ ) at  $E_h$  calculated for the  $n_{98\%}$  first pulses only and;
- The mean charge passed per pulse ( $Q_{mean}$ ) calculated for the  $n_{98\%}$  first pulses only.

As shown in Table 1,  $Q_{tot}$  increased with increasing  $t_h$  which was anticipated since, at equal pulses, the total time maintained at  $E_h$  is higher for longer  $t_h$ . Initially,  $n_{98\%}$  increased with increasing  $t_h$ , although it stabilized for  $t_h = 2 \text{ s}$  and  $4 \text{ s}$ . The  $j_{mean}$  increased with increasing  $t_h$ , though, this increase is non-linear and diminishes when  $t_h$  was greater than  $2 \text{ s}$ . As expected,  $Q_{mean}$  increases with increasing  $t_h$  as longer pulses allow greater charge transfer.

Post PPT OM of the surfaces for the four  $t_h$  durations are shown in Supplementary Fig. 4. Multiple pits were clearly evident and

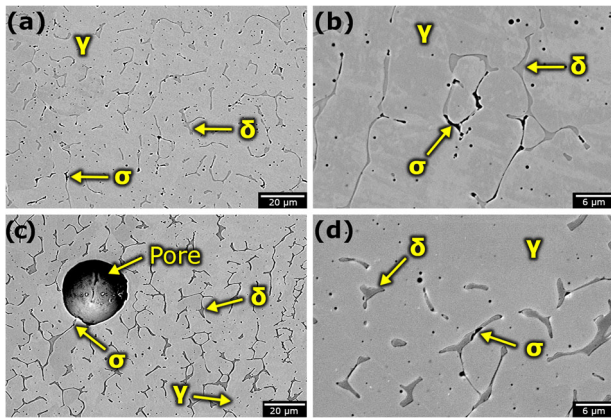


**Fig. 3 SEM of WAAM stainless steel ER316L after electro-etching in 40% NaOH. Wall B1 (a, b) and wall B2 (c, d).**

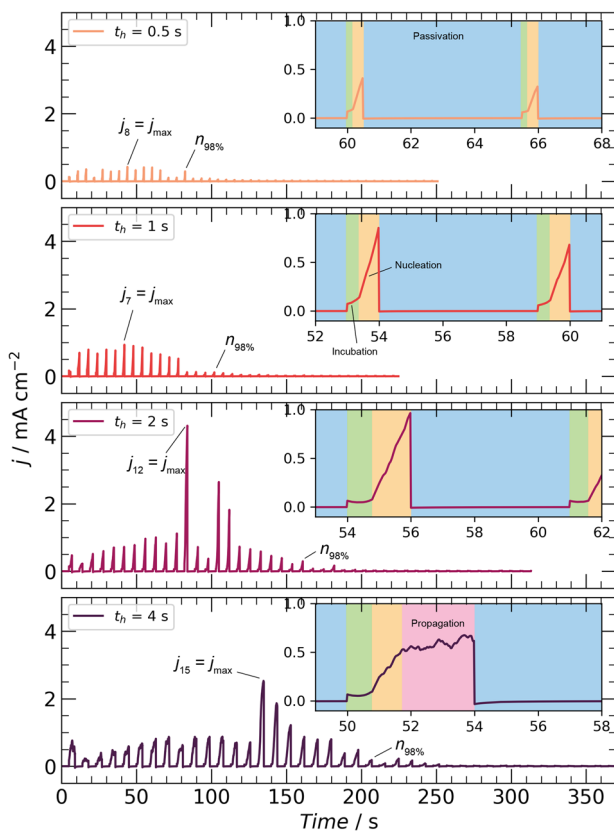


**Fig. 4 WAAM stainless steel ER316L PPT current density profiles for the four  $t_h$  durations in a  $N_2$  purged 1 M NaCl solution at 40 °C. Insets on the top right-hand side of each graph zoom on a representative pulse. Various stages are evident during individual pulses and are identified within the insets, i.e., incubation (green), nucleation (yellow), propagation (pink) and passivation (blue). Other PPT parameters:  $E_h = +450$  mV,  $E_i = -160$  mV, and  $t_i = 5$  s.**

their size increased with increasing  $t_h$  correlating with increasing  $Q_{tot}$ ,  $j_{mean}$  and  $Q_{mean}$  as previously discussed.

Figure 5 shows the pit distribution after the post processing. The pit distribution was skewed for all  $t_h$ ; however, the distribution tail increased with increasing  $t_h$  suggesting the pits were larger confirming the observations from Supplementary Fig. 4. The pit density and the mean pit mouth diameter (size) were calculated from the pit detection data and reported in Table 1, together with  $Q_{pit}$  (average charge per pit given by the  $Q_{tot}$  to pit density ratio).

The pit density was similar for  $t_h = 0.5$  s and  $t_h = 1$  s, and likewise for  $t_h = 2$  s and  $t_h = 4$  s, which suggests the pit density was independent of the high potential step time. The mean pit size for 0.5 s and 1 s were also comparable, whereas the mean pit size for 2 s and 4 s was significantly higher and thus confirms pits were larger with increasing  $t_h$ .

The pit density and the mean pit size for 0.5 s and 1 s are offset due to a significant number of the pits being below the detection threshold of  $10 \mu m^2$ . This explains why the pit density and mean pit size were equal despite  $Q_{tot}$ ,  $j_{mean}$ ,  $Q_{mean}$  and  $n_{98\%}$  being higher for  $t_h = 1$  s. Hence, a minimum time of 2 s is necessary to ensure good pit detection using OM. The  $t_i = 5$  s was sufficient to passivate initiated pits efficiently.

### Influence of interpass temperature on WAAM pit nucleation

PPT were performed on B1, B2 WAAM ER316L walls and wrought 316L specimens at two high potentials ( $E_h = +450$  mV and  $+600$  mV), with the other parameters remaining fixed: i.e.,  $E_i = -160$  mV,  $t_h = 2$  s,  $t_i = 5$  s and  $T_{sol} = 40$  °C. Figure 6 shows the current density profiles during the PPT tests and the evaluated  $Q_{tot}$ ,  $n_{98\%}$ ,  $j_{mean}$ ,  $Q_{mean}$  and  $Q_{pit}$  parameters are summarized in Table 1. At  $+450$  mV, the current density amplitude of each pulse ( $j$ ) follows a similar trend as described previously, with  $j$  increasing up to a maxima ( $j_{max}$ ) before returning to a negligible baseline ( $<0.1$  mA cm $^{-2}$ ). The  $n_{98\%}$  was the same for B1 and B2 WAAM ER316L, but higher for the wrought 316L. The PPT pulses were significantly more intense for B1 compared to both B2 and the wrought alloy:  $j_{max}$  reached 5 mA cm $^{-2}$  in B1, but only 0.5 mA cm $^{-2}$  and 0.3 mA cm $^{-2}$  in B2 and the wrought alloy, respectively. Additionally,  $Q_{tot}$ ,  $j_{mean}$  and  $Q_{mean}$  were sixfold higher in B1 compared to B2, associated with a significantly higher pitting activity. Conversely, current density profiles at  $+600$  mV were more intense. Initially,  $j_{max}$  was 11.9 mA cm $^{-2}$ , 8.1 mA cm $^{-2}$  and 1.2 mA cm $^{-2}$  and occurred on the second, third and first pulse in B1, B2 and the wrought alloy, respectively; whereas at  $+450$  mV,  $j_{max}$  was delayed occurring on the 8<sup>th</sup>, 9<sup>th</sup> and 6<sup>th</sup> pulse in B1, B2 and the wrought alloy, respectively. Additionally, the pulse intensity returned to the baseline faster at  $+600$  mV than at  $+450$  mV:  $n_{98\%}$  were 12, 9 and 6 for B1, B2 and the wrought alloy, respectively. However, despite fewer active pulses, specimens at  $+600$  mV had significantly higher  $Q_{tot}$ ,  $j_{mean}$ , and  $Q_{mean}$  than at  $+450$  mV, this suggests they had a higher pitting activity, and this activity was focused within the first few pulses.

Interestingly, the difference in PPT pulse intensity between B1 and B2 at  $+450$  mV was not as pronounced than at  $+600$  mV: parameters  $Q_{tot}$ ,  $j_{mean}$  and  $Q_{mean}$  for B1 and B2 were similar at  $+600$  mV. Nevertheless, B1 had a higher  $Q_{tot}$  but a lower  $j_{mean}$  and  $Q_{mean}$  compared to B2. The current density profiles of wrought 316L were in marked contrast with those of the WAAM ER316L specimens, the pulses intensity was significantly lower at both  $E_h = +450$  mV and  $+600$  mV compared to B1 and B2 and indicates the wrought specimens had a comparatively reduced pitting activity. Figure 7 shows the pit distributions, the corresponding pit density, mean pit size and  $Q_{pit}$  are reported in Table 1. The pit distribution was skewed for B1 and B2 specimens akin to what was observed previously. The tail was longer at  $E_h = +600$  mV indicating larger pits, which was anticipated since the active pit dissolution rate should increase with the potential, the pit density was also higher at  $E_h = +600$  mV in B1 and B2. The wrought 316L had significantly lower pit density compared to the WAAM specimens which confirms the observations made from the PPT current density profiles (Fig. 6). In fact, the pit density difference with B1 and B2 was such that the pit distribution was shown separately in the Supplementary Fig. 5 for better clarity.

The pitting activity was clearly different between B1 and B2 at  $+450$  mV. The B1 specimen had a significantly higher pit density, i.e., 4.2 times higher than B2, and a higher pit size which was

**Table 1.** Calculated  $Q_{tot}$ ,  $n_{98\%}$ ,  $j_{mean}$ ,  $Q_{mean}$ , pit density, pit size and  $Q_{pit}$  from PPT experiments for B1, B2 WAAM stainless steel ER316L and wrought 316L at different  $t_h$  durations and  $E_h = +450$  mV and  $+600$  mV.

Specimen	$t_h/s$	$Q_{tot}/mC\ cm^{-2}$	$n_{98\%}$	$j_{mean}/mA\ cm^{-2}$	$Q_{mean}/mC\ cm^{-2}$	Pit density/ $mm^{-2}$	Mean pitsize/ $\mu m^2$	$Q_{pit}/\mu C$
B1-H1	0.5	1.13	15	0.154	0.08	45.3	21	0.2
B1-H2	1	4.28	17	0.259	0.26	42.2	21	1.0
B1-H3	2	17.21	23	0.383	0.76	87.8	54	2.0
B1-H4	4	40.33	23	0.445	1.79	87.3	75	4.6
B1 450 mV	2	26.77	18	0.755	1.53	101.0	44	2.6
B2 450 mV	2	4.47	18	0.127	0.25	23.7	27	1.9
Wrought 450 mV	2	1.91	25	0.039	0.08	1.4	80	10
B1 600 mV	2	48.47	12	2.148	4.30	173.2	58	2.8
B2 600 mV	2	40.35	9	2.478	4.94	109.7	62	3.7
Wrought 600 mV	2	3.32	6	0.321	0.64	1.4	200	23

consistent with current density data from Fig. 6 confirming that B1 had a higher pitting activity than B2 at  $+450$  mV. The pitting activity between B1 and B2 was similar at  $+600$  mV, i.e., comparable pit density with B1 only 1.6 times that of B2 and comparable pit sizes, which was also consistent with current density data. Nevertheless, B1 exhibited a higher pitting activity than B2 at  $E_h = +600$  mV; however, the difference was less pronounced than at  $E_h = +450$  mV.

The wrought 316L pit distribution was unskewed and overall significantly dissimilar from the pit distributions of B1 and B2. The pit sizes were larger, for example, higher max pit size and mean pit size, and the pit density was one to two orders of magnitude lower than those for WAAM indicating that the pit nucleation mechanism differs. Additionally,  $Q_{pit}$  was significantly higher, confirming that the wrought 316L had fewer but bigger pits than WAAM ER316L. The pit density of the wrought alloy was also equal at  $E_h = +450$  mV and  $+600$  mV, further contrasting with the WAAM specimens.

SEM of post PPT pits for WAAM ER316L B1 and B2, and wrought 316L is shown in Fig. 8. Overall, the SEM corroborated well with pit distribution data from OM, for instance, smaller but more numerous pits for WAAM ER316L and fewer but larger pits for the wrought 316L. All pits propagated in the austenite phase. A minority of pits were in the austenite for both WAAM B1 and B2; such a pit is shown in Fig. 8b, designated as an austenite pit, and recognizable by its hemispherical and featureless morphology akin to wrought 316L pits (Fig. 8f). However, many features were evident in the majority of WAAM pits which were related to secondary phases. For a few pits, the nucleation site was identified as sigma phase such as in Fig. 8b; however, the nucleation location was unclear for many of the pits due to the subsequent pit propagation and/or the inability to identify the secondary phase nature (i.e., ferrite or sigma) such as in Fig. 8d.

To better identify the WAAM ER316L pit nucleation sites, post-PPT EBSD analysis was performed on a B1 specimen specifically prepared. PPT was performed at  $+450$  mV and at a shorter  $t_h$  (1 s) to limit the pit propagation. Figure 8g–j shows EBSD of two representative post PPT corrosion pits. In both pits, sigma phase was clearly identified as the pit nucleation site.

## DISCUSSION

The current density is uniform across the pit surface with hemispherical shape, similar to those observed in wrought specimens. Frankel et al.<sup>27</sup> studied metastable pits with a similar profile (i.e., hemispherical with a growth time of less than 5 s and a pit diameter between 1  $\mu m$  and 10  $\mu m$  in 304 stainless steel) and found that the pits were predominantly under active dissolution, rather than diffusion-controlled. This is evident in the increase in

pit size at higher potentials. The hemispherical pits studied by Frankel et al.<sup>27</sup> exhibited a constant radial growth, resulting in a current that increased linearly with  $t^2$ . Non-hemispherical pits observed in WAAM specimens, which were caused by the presence of secondary phases such as ferrite and sigma hindering the propagation, likely exhibit a more complex pit current density that does not increase linearly with  $t^2$ . It is reasonable to assume, however, that these pits also undergo active dissolution, as evidenced by the increase in pit size at higher potentials, as seen in Fig. 7.

Each pulse consists of four stages: incubation, nucleation, propagation during the applied  $E_h$ , and finally passivation during  $E_i$  (see Fig. 4 and illustration in Fig. 9a). The initial incubation stage (highlighted in green) is characterized by a current density plateau after an initial transient due to surface charging effects when the potential switches from  $E_i$  to  $E_h$ . During this stage the current density remains low indicating that pits need time to nucleate. The incubation time increases during the PPT test which may be a consequence of oxide film change (thickening and more complete/defect free) and depletion of the most susceptible nucleation sites. The nucleation stage (orange region) has a marked current density increase and is influenced by the number of initiating pits: the individual contribution of each pit to the net current density increases with size. Finally, propagation (pink region) only occurs if  $t_h$  is of a sufficiently duration. Figure 4 shows the current density profile of a single pulse at  $t_h = 4$  s stabilized passed a critical time, whereas no such stabilization was observed at  $t_h \leq 2$  s. Since the pit density and  $n_{98\%}$  at  $t_h = 2$  s and  $t_h = 4$  s was the same, no more pits were initiated during the propagation stage. Thus, the self-passivation rate of the WAAM metastable pits likely surpasses the pit nucleation rate close to 2 s, resulting in a current density stabilization due to an equilibrium between decreasing active pit number versus increasing current density from growing pits. The passivation stage (blue region) initiates immediately on the transition from  $E_h$  to  $E_i$  as indicated by a sharp decrease in the current density. After a sufficient number of PPT pulses ( $n_{98\%}$ ), no further pits initiate and the surface remains passive (Fig. 9b). This corroborates studies by Chen et al.<sup>28</sup> where PPT revealed susceptible pit sites were independent of both  $t_h$  and the pulse number, as such the passive state predominates once the available nucleation sites are activated. However,  $n_{98\%}$  increased with  $t_h$  between 0.5 s and 2 s, and was stable thereafter, which means that  $t_h$  has an influence on  $n_{98\%}$ , and ultimately on the pit density below 2 s. This could be explained by the increasing incubation time surpassing  $t_h$  prematurely if  $t_h$  is too low (Fig. 9a). The surface is passive at low time steps that are too short for pit nucleation and result in a low  $n_{98\%}$  and pit density. An appropriate time step of 2 s is required to consistently activate the nucleation sites and observe the same behaviour as reported by

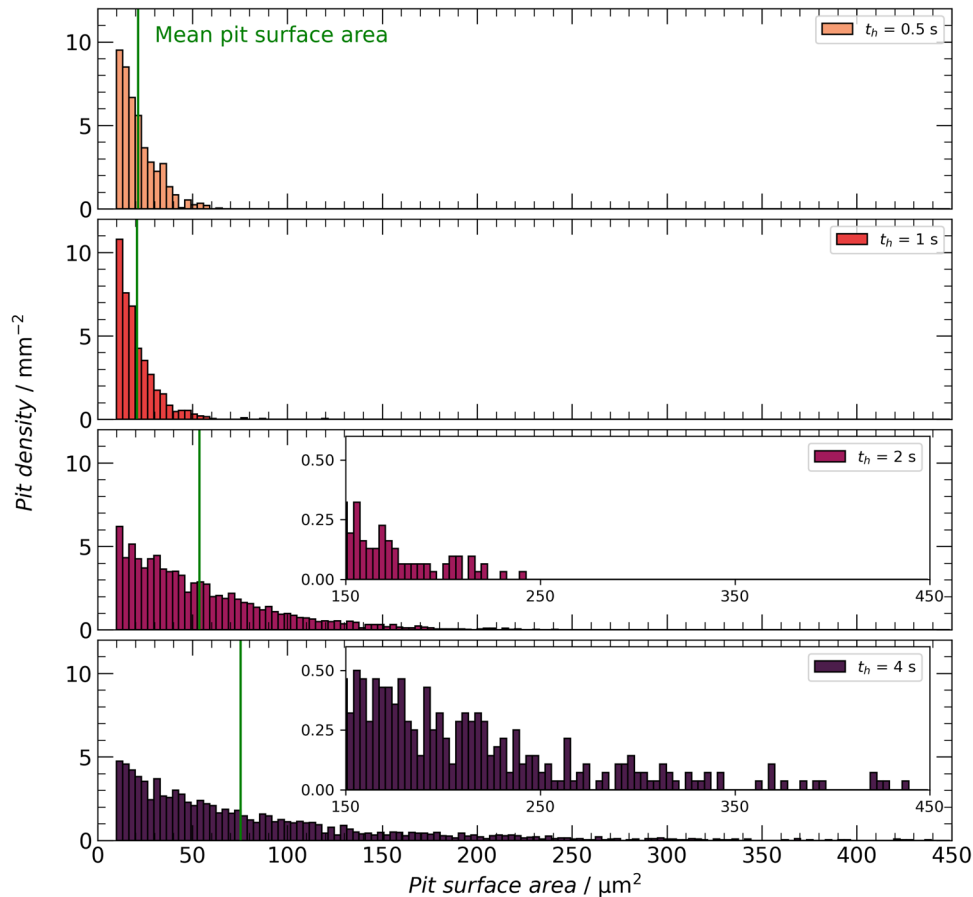


**Fig. 5** WAAM stainless steel ER316L pit distributions after PPT for the four  $t_h$  durations in a  $N_2$  purged 1 M NaCl solution at 40 °C. Other PPT parameters:  $E_h = +450$  mV,  $E_l = -160$  mV, and  $t_l = 5$  s. Bin size:  $3.3 \mu\text{m}^2$ .

Chen et al.<sup>28</sup> (i.e., pit density independent of pulse number and step time). Figure 9b shows a schematic of the current density and potential profiles during a PPT test performed with optimum parameters. Figure 9c also shows a schematic of the specimen surface at different test stages: pits initiate during the first pulses and cease to initiate after  $n_{98\%}$  (grey zone in Fig. 9b),  $t_h$  is also appropriately short to limit the propagation stage, thus allowing for better nucleation site identification.

SEM and Feritscope measurements showed the B1 wall had a low ferrite content and a high sigma content (c.f. with the B2 wall), suggesting that a higher ferrite proportion decomposed into austenite and sigma after solidification<sup>29,30</sup>. The higher B1 interpass temperature led to heat accumulation within the wall build, thus maintaining the sigma forming temperature (between 600 °C and 900 °C<sup>29,31</sup>) for a longer period. A given point within the B2 build will have a lower cumulative time spent within the sigma forming domain compared to an equivalent point within B1 associated to its lower interpass temperature limiting the heat accumulation and increasing the cooling rate. Additionally, the sigma phase size increases with increasing time in the sigma forming temperature range since sigma phases were larger in the B1 wall.

The WAAM B1 and B2 pit activity is directly linked to the sigma phase formation, since the pitting activity increases with increasing sigma content (i.e., higher in B1) and sigma is well-known to be detrimental for the corrosion resistance of stainless steels by further increasing the elemental segregation of Cr and Mo<sup>29,32–35</sup>. Additionally, pits initiating at the sigma/austenite interface were evident which was also reported by Sun et al.<sup>18</sup> in 317L indicating that sigma can act as a pit nucleation site. Jang et al.<sup>30</sup> also

reported for an AISI 316L weld that  $E_{\text{pit}}$  decreased with increasing sigma phase content and concluded that the sigma content influenced the pitting potential. Likewise, Yongqiang et al.<sup>36</sup> examined three duplex stainless steels (SAF2205, SAF2507 and Z3CN20.09M) and concluded that the influencing factor for the  $E_{\text{pit}}$  decrease was the degree of the chromium difference between the sigma phase and depleted matrix, rather than the extensive number of sigma precipitates. From the published literature, the depassivation potential of an individual sigma nucleation site varies depending on the degree of elemental segregation on the immediately adjacent austenite matrix, and at the specimen scale, pits will initiate over a wider potential range. These observations are consistent with the B1 and B2 PPT data, since the pit density increased with increasing  $E_h$ , thus demonstrating that greater depassivation of sigma nucleation sites. The intensity of elemental segregation caused by sigma precipitation is qualitatively estimated by assessing the pit density at different  $E_h$ . Higher pit density at lower  $E_h$  indicates an increased elemental segregation. Therefore, B1 has a more pronounced elemental segregation at its sigma nucleation site compared to B2 since the pit density was higher at +450 mV. Accordingly, the pit density difference reduces at  $E_h = +600$  mV since the higher potential mitigates the elemental segregation effect and most nucleation sites are activated in both B1 and B2 regardless of the degree of elemental segregation. The sigma phases were larger in B1 suggesting that elemental segregation is correlated to the sigma phase size and by extension to the interpass temperature. Ultimately, the pitting susceptibility (depassivation potential of the nucleation sites) of the WAAM ER316L increases with increasing interpass temperature due to greater elemental segregation caused by the growth

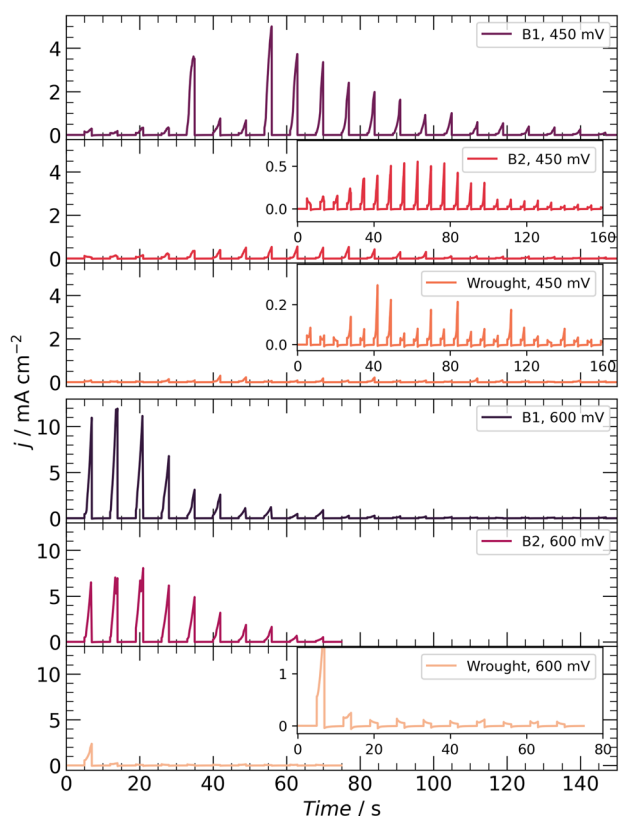


**Fig. 6** PPT current density profiles for B1, B2 WAAM stainless steel ER316L and wrought 316L at both  $E_h = +450$  mV and  $+600$  mV in a  $N_2$  purged 1 M NaCl solution at  $40^\circ\text{C}$ . Insets on the top right-hand side of each graph plot the current density profile with a smaller y-axis. Other PPT parameters:  $E_i = -160$  mV,  $t_h = 2$  s, and  $t_i = 5$  s.

of sigma phases. nucleation sites were not limited to sigma phase sites, with a small number of pits initiating in the austenite as well, requiring more investigation.

The PPT results indicate that there are differences in the pit nucleation mechanisms between WAAM ER316L and wrought 316L. The WAAM ER316L has high pit densities, which are indicative of a large number of depassivation events, while the wrought 316L has lower pit density (one to two orders of magnitude lower) but with larger pit size. Furthermore, the pit density for the wrought 316L remains stable between  $+450$  mV and  $+600$  mV, while the pit density for WAAM ER316L increases significantly. This suggests that the pit nucleation sites for the wrought 316L are of a different nature compared to those of the WAAM ER316L. These sites may include MnS inclusions in the wrought 316L, which have been extensively studied for their role in pit nucleation and propagation<sup>37–39</sup>. MnS inclusions lower the pitting potential and enhance the dissolution rate of the metal<sup>40–42</sup>, thereby explaining the larger pit size for the wrought. The stable pit density between  $+450$  mV and  $+600$  mV for the wrought indicates that the nucleation sites activate below  $+450$  mV which could potentially be MnS inclusions. Additionally, the presence of MnS inclusions large enough to initiate pitting is not commonly reported for WAAM deposited 316L. Only small MnS sub-inclusions ( $<0.18\ \mu\text{m}$ ) embedded within larger manganese silicates were reported<sup>43–45</sup>. This was attributed to the rapid cooling rate of the WAAM process and the use of Si and Mn enriched welding wires preventing MnS precipitation, instead replaced by sub-micron manganese silicates. The wrought 316L has fewer potential pit nucleation sites that depassivate at low potentials, whereas WAAM ER316L contains a high density of pit

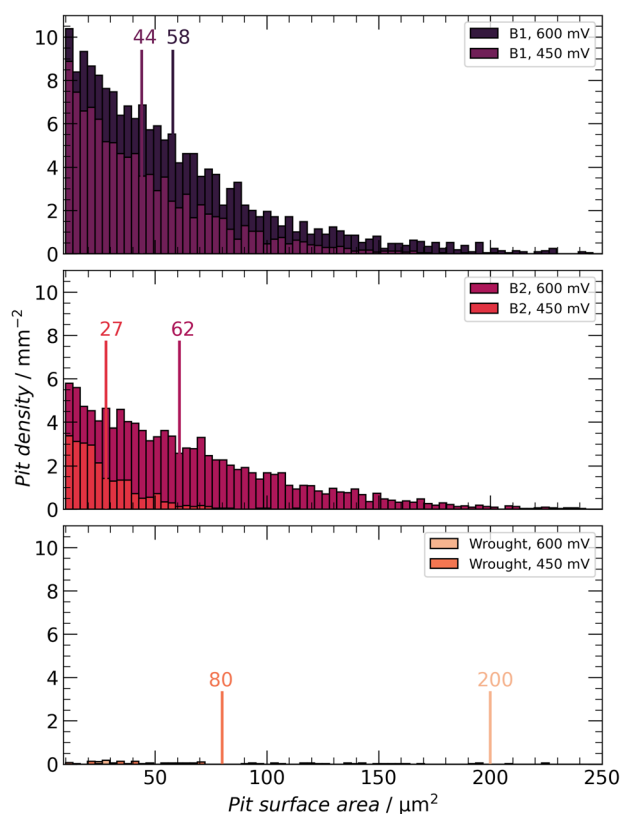


**Fig. 7** PPT pit distributions for B1, B2 WAAM ER316L stainless steel and wrought 316L at both  $E_h = +450$  mV and  $+600$  mV in a  $N_2$  purged 1 M NaCl solution at  $40^\circ\text{C}$ . Vertical lines indicate the mean pit size. Other PPT parameters:  $E_i = -160$  mV,  $t_h = 2$  s,  $t_i = 5$  s. Bin size:  $3.3\ \mu\text{m}^2$ .

nucleation sites that progressively activates with increasing potential.

The high depassivation rate and metastable activity characterizing WAAM ER316L become increasingly problematic with more aggressive environments due to the synergistic effect of two factors. Firstly, as demonstrated by the PPT results, the frequency of depassivation events increases with the potential, which is representative of the environment's aggressiveness. Secondly, repassivation is more difficult in aggressive environments due to increased dissolution rates. The combination of these two effects significantly increases the likelihood of forming a stable pit in more aggressive environments for the WAAM ER316L. On the other hand, the wrought 316L comparatively performs better in more aggressive environments since one of the previously described effects (i.e., depassivation event increase) does not occur or occurs to a much lesser extent, as demonstrated by the stable pit density between  $+450$  mV and  $+600$  mV in the PPT results.

These results raise several questions regarding the implementation of WAAM for the fabrication of large SS316L components. One of the main concerns for the structural integrity of conventional SS316L components in corrosive environments is pitting, which has a stochastic nature since it is caused by the uncontrolled occurrence of MnS inclusions. The WAAM ER316L is also subject to pitting although its stochastic nature is fundamentally different, exhibiting numerous potential nucleation sites due to its non-equilibrium microstructure, causing high metastable activity. In laboratory conditions, the chances that one of the numerous depassivation events develops into a stable pit are reduced by the greater stability of the environmental variables such as the electrolyte concentration, temperature, and flat

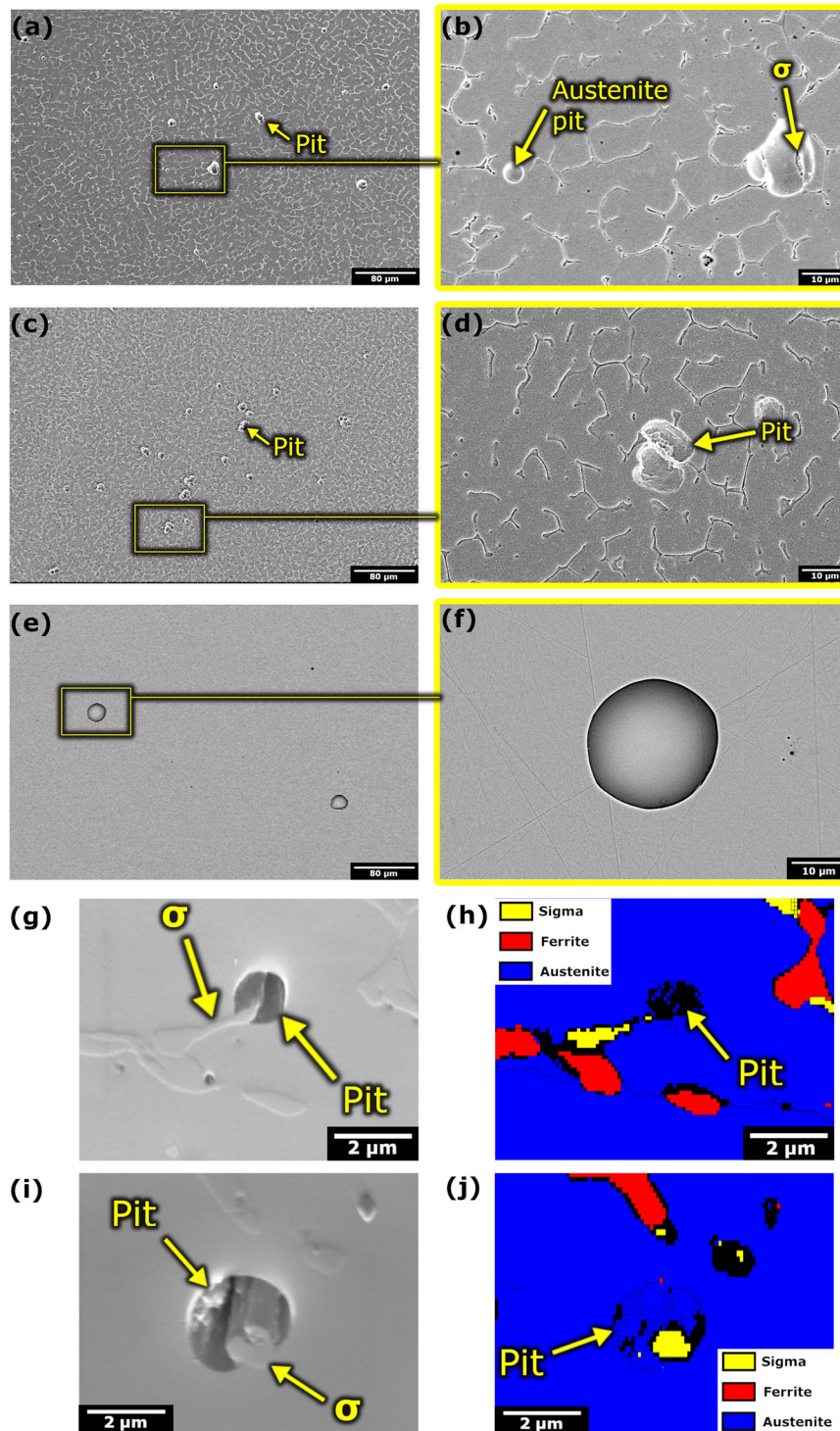


**Fig. 8** Post PPT SEM and EBSD of corrosion pits. **a–f** SEM of corrosion pits post PPT testing at  $E_h = +600$  mV,  $t_h = 2$  s; **a, b** WAAM stainless steel ER316L B1; **c, d** WAAM stainless steel ER316L B2; **e, f** wrought 316L stainless steel. **g, i** SEM and **h, j** EBSD phase map of corrosion pits post PPT testing at  $E_h = +450$  mV,  $t_h = 1$  s.

polished surfaces. However, in service conditions, these variables are often uncontrolled, and local aggressive environments may develop due to the geometry of the part or directly caused by external factors. In such scenarios, the probability of developing a stable pit is higher for the WAAM ER316L compared to conventional wrought 316L due to the increased likelihood of

the aggressive local environment coinciding with a potential nucleation site in the WAAM ER316L. Consequently, during the design stage of WAAM ER316L components, greater attention should be directed towards anticipating and mitigating aggressive environmental conditions, as these are the primary concerns in the context of WAAM ER316L. In contrast, for the conventional



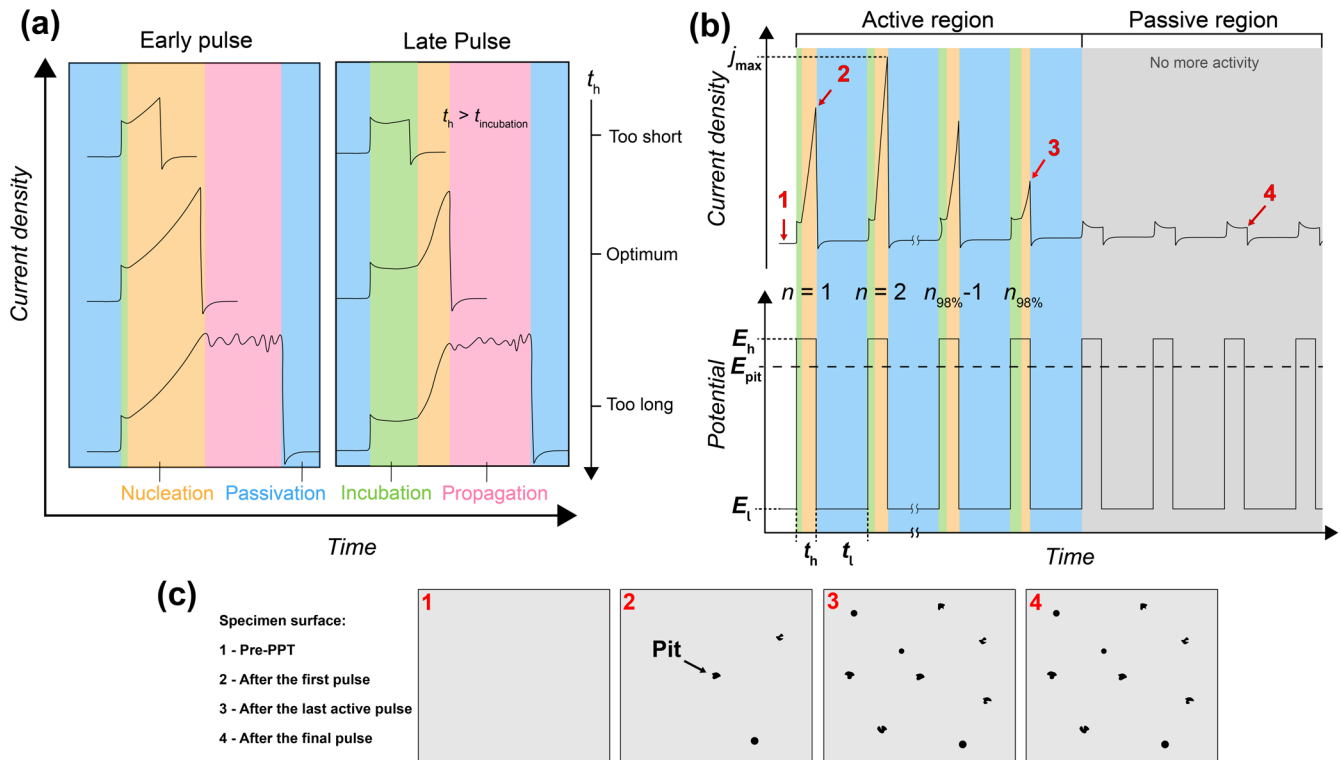


**Fig. 9 Schematic of a PPT test.** **a** Single pulse current density profiles at the start (first pulse) and end (second pulse); **b** current density and potential profiles during a PPT test performed with optimum parameters:  $E_h$ ,  $t_h$ ,  $E_l$  and  $t_i$ ; and **c** specimen surface states for the four stages.

wrought counterpart, the stochastic occurrence of pit nucleation sites is relatively rarer, making it the limiting factor in terms of localized corrosion susceptibility.

The results of this study shows that suitable deposition parameters may reduce the metastable activity. Heat accumulation must be controlled to limit the time spent within the 600–900 °C temperature range. Presently, this has been achieved by lowering the interpass temperature to 70 °C by pulsed air cooling, although it increases the deposition time. Alternative means, such as in-process cooling, may circumvent this issue<sup>11,46</sup>. PPT has proven efficient in studying the pit nucleation and may be used as a quick means to assess sigma precipitation and elemental segregation in WAAM ER316L.

An innovative approach using PPT was implemented to study the pitting corrosion of WAAM deposited stainless steel ER316L and wrought 316L. PPT current densities were used to reveal the different pitting behaviour between the WAAM ER316L and wrought 316L and to understand the role of interpass temperature. Critically, the influence of key parameters, namely the high potential pulse and time step, need to be appropriately optimised within the test protocols. PPT was shown to be particularly well-adapted to study the WAAM ER316L pitting behaviour, in comparison with either PDP or CPT allowing the following considerations.

- A key insight for WAAM ER316L is that the interpass temperature influences the solid-state transformation of the ER316LSS. Uncontrolled interpass temperature leads to heat accumulation within the part and maintain the material within the 600–900 °C range causing elemental segregation and precipitation of sigma phase. Therefore, it is crucial to maintain the interpass temperature as low as possible. Here, a temperature of 70 °C decreased the sigma content from an estimated 1.1% to 0.2%.
- The wall of B2 built with the interpass control had the superior pitting resistance compared to the wall of B1 built with non-

interpass control, the result is attributed to a reduction in sigma size with largest phases >15 μm in B1 and <4 μm in B2. The sigma phase acts as pit nucleation sites and the depassivation potential of these sites decreases with increasing sigma size which enhances elemental segregation.

- WAAM ER316L and the wrought 316L exhibited different pitting mechanisms, linked with microstructural nucleation sites: WAAM ER316L has a high density of mixed austenite and sigma nucleation sites, whereas the wrought 316L has a low density of sites with high dissolution rates attributed to MnS inclusions.

The metastable pitting activity of WAAM ER316L is the main concern for its corrosion resistance and tightly linked to the deposition parameters such as the interpass temperature. Hence, the design stage for the fabrication of large SS316L components using WAAM needs to be adapted accordingly to avoid the structural integrity risk posed by the higher likelihood of forming stable pits in uncontrolled, aggressive environments.

## METHODS

### WAAM wall deposition and specimen extraction

Two WAAM ER316L walls (180 mm × 90 mm × 40 mm), designated as B1 and B2 (see Supplementary Fig. 6), were deposited using a Metal Inert Gas/Metal Active Gas (MIG/MAG) welding torch, a TPS 4000 CMT Advanced power source and a Fanuc Arc Mate 120ic robot. The feedstock was a conventional ER316L 1.2 mm diameter welding wire from IABCO and its chemical composition is given in the Supplementary Table 1.

The welding torch scanned in a reciprocating pattern and the deposition parameters are listed in the Supplementary Table 2. Wall B1 was deposited without interpass cooling, whereas wall B2 was cooled after the deposition of each layer using pulsed air on the build until the top surface temperature dropped to 70 °C. The temperature of 70 °C was chosen as the lowest temperature

reachable in a timely manner (few minutes) in order to achieve maximum cooling rate<sup>47</sup>. The interpass temperature for each layer in both walls was assessed at the top surface of the deposited layer immediately before deposition of a new layer using a conventional contact probe thermometer. The interpass temperature profiles for both walls are shown in the Supplementary Fig. 7. Test specimens were extracted from the B1 and B2 walls according to Supplementary Fig. 6. Specimens denoted “H” (for Horizontal) had a surface of interest parallel to the (z, x) plane and specimens denoted “V” (for Vertical) had their surface of interest parallel to the (x, y) plane.

### Surface preparation

Specimens were wet ground using 120, 360, 600, 1200, and 2500 grit SiC papers and polished using oil-based diamond suspensions of 3  $\mu\text{m}$  and 1  $\mu\text{m}$  prior to surface characterization and/or testing. Specimens were degreased with acetone and cleaned in methanol for 5 min in an ultrasonic bath. A few specimens were electrochemically etched at 6 V for 25 s in a 40% NaOH solution to reveal the ferrite and sigma phases. To show the grain and dendrite texture, some specimens were electrochemically etched at 4 V in a 20% H<sub>2</sub>SO<sub>4</sub> solution for a few seconds instead. Specimen surfaces and microstructures were studied using an Olympus optical microscope (OM) and a ZEISS Sigma SEM equipped with EBSD. EBSD specimens were polished using a colloidal silica suspension (0.04  $\mu\text{m}$ ) and cleaned with acetone and a microfibre cloth prior to the analysis. The ferrite phase content was determined using a Fischer FMP30 Feritscope.

### Electrochemical tests

Electrochemical tests were performed using an ACM Gill AC potentiostat and a three-electrode set up, the counter electrode was a platinum coated titanium rod and the reference electrode was a Saturated Calomel Electrode (SCE). The test solution temperature was controlled via a heating/cooling jacket around the cell connected to a temperature controller. The temperature was constantly monitored using a K-type thermocouple immersed into the solution. The specimens were left in ambient air for at least 24 h to allow an air-formed oxide film to condition before corrosion testing.

Specimens were masked with 45 stopping-off lacquer leaving an exposed area of approximately 0.3 cm<sup>2</sup>. An OM survey of the test surfaces was taken prior to the PPT test, as shown in Supplementary Fig. 8. PPT tests were performed in a N<sub>2</sub> purged 1 M NaCl solution. The key test parameters include solution temperature ( $T_{\text{sol}}$ ), high potential ( $E_{\text{H}}$ ), low potential ( $E_{\text{L}}$ ), high potential step time ( $t_{\text{H}}$ ) and low potential step time ( $t_{\text{L}}$ ). After testing, the lacquer masking was removed and specimens were cleaned using methanol in an ultrasonic bath for 5 min, after which a full OM surface survey was performed again as shown in Supplementary Fig. 9. Visible surface features appearing after PPT were classified as pits. The pit density was then calculated as the number of visible pits on the surface divided by the exposed surface area.

PPT data analysis included OM pit detection and count of pits initiated during the multiple nucleation phases, as well as analysing the current density response during each test. Each nucleation phase only lasted for a few seconds. Therefore, pits did not propagate but remained within the nucleation stage. The pits were detected and characterized from the pit area visible by OM. The OM images were converted to binary mode and analysed using the Matlab built-in Image Segmentation application from the Image Processing Toolbox to isolate visible features from the background and return a list of surface areas, each one corresponding to a detected feature. To differentiate between corrosion pits and any other features (i.e., inclusions, porosities or cracks), pre-PPT images were also analysed and each feature detected was subtracted from the post PPT feature closest in size (with a maximum difference of

10% of the feature size). The resulting surface area list was considered to be the true pit distribution. The pit density and the average pit size were then derived from the pit distribution. The contribution from non-faradaic current (i.e., surface charging/discharging effect) to the total current was considered constant between tests using the same parameters. Thus, the positive current density was integrated over time to obtain the electric charge ( $Q$ ; units C cm<sup>-2</sup>) over the time period and was considered to reflect the net charge due to the oxidation kinetics. A more detailed description of the data analysis process is provided in the Supplementary Methods.

### DATA AVAILABILITY

The datasets generated during and/or analysed during the current study are available from the corresponding author on reasonable request.

Received: 3 May 2023; Accepted: 23 October 2023;  
Published online: 11 November 2023

### REFERENCES

- Frazier, W. E. Metal additive manufacturing: a review. *J. Mater. Eng. Perform.* **23**, 1917–1928 (2014).
- Cunningham, C. R., Flynn, J. M., Shokrani, A., Dhokia, V. & Newman, S. T. Invited review article: strategies and processes for high quality wire arc additive manufacturing. *Addit. Manuf.* **22**, 672–686 (2018).
- Wu, B. T. et al. A review of the wire arc additive manufacturing of metals: properties, defects and quality improvement. *J. Manuf. Process.* **35**, 127–139 (2018).
- Jin, W. et al. Wire arc additive manufacturing of stainless steels: a review. *Appl. Sci.* **10**, 1563 (2020).
- Taşdemir, A. & Nohut, S. An overview of wire arc additive manufacturing (WAAM) in shipbuilding industry. *Ships Offshore Struct.* **16**, 1–18 (2020).
- Chen, X. et al. Microstructure and mechanical properties of the austenitic stainless steel 316L fabricated by gas metal arc additive manufacturing. *Mater. Sci. Eng. A* **703**, 567–577 (2017).
- Rodriguez, N. et al. Wire and arc additive manufacturing: a comparison between CMT and TopTIG processes applied to stainless steel. *Weld. World.* **62**, 1083–1096 (2018).
- Wang, L. L., Xue, J. X. & Wang, Q. Correlation between arc mode, microstructure, and mechanical properties during wire arc additive manufacturing of 316L stainless steel. *Mater. Sci. Eng. A Struct. Mater. Prop. Microstruct. Process.* **751**, 183–190 (2019).
- Wu, W. et al. Forming process, microstructure, and mechanical properties of thin-walled 316L stainless steel using speed-cold-welding additive manufacturing. *Metals* **9**, 109 (2019).
- Wu, W., Xue, J., Zhang, Z. & Yao, P. Comparative study of 316L depositions by two welding current processes. *Mater. Manuf. Processes* **34**, 1–7 (2019).
- Cunningham, C. R., Dhokia, V., Shokrani, A. & Newman, S. T. Effects of in-process LN<sub>2</sub> cooling on the microstructure and mechanical properties of type 316L stainless steel produced by wire arc directed energy deposition. *Mater. Lett.* **282**, 128707 (2021).
- Palmeira Belotti, L. et al. Microstructural characterisation of thick-walled wire arc additively manufactured stainless steel. *J. Mater. Process. Technol.* **299**, 117373 (2022).
- Chen, X., Li, J., Cheng, X., Wang, H. & Huang, Z. Effect of heat treatment on microstructure, mechanical and corrosion properties of austenitic stainless steel 316L using arc additive manufacturing. *Mater. Sci. Eng. A* **715**, 307–314 (2018).
- Yang, K., Wang, Q., Qu, Y., Jiang, Y. & Bao, Y. Microstructure and corrosion resistance of arc additive manufactured 316L stainless steel. *J. Wuhan Univ. Technol. Mat. Sci. Ed.* **35**, 930–936 (2020).
- Wen, D., Long, P., Li, J., Huang, L. & Zheng, Z. Effects of linear heat input on microstructure and corrosion behavior of an austenitic stainless steel processed by wire arc additive manufacturing. *Vacuum* **173**, 109131 (2019).
- Queguineur, A., Rückert, G., Cortial, F. & Hascoët, J. Y. Evaluation of wire arc additive manufacturing for large-sized components in naval applications. *Weld. World.* **62**, 259–266 (2018).
- Racot, A., Aubert, I., Touzet, M., Thiebaut, S. & Demesy, M. Statistical analysis of the pitting corrosion induced by potentiostatic pulse tests of wrought and SLM 316L stainless steels. *Corros. Sci.* **197**, 110036 (2022).

18. Sun, Y. et al. Application of potentiostatic pulse technique and statistical analysis in evaluating pitting resistance of aged 317L stainless steel. *Mater. Corros.* **71**, 900–908 (2020).
19. Pound, B. G. Hydrogen trapping in precipitation-hardened alloys. *Acta Metall. Mater.* **38**, 2373–2381 (1990).
20. Pound, B. G. Potentiostatic pulse technique to determine the efficiency of hydrogen absorption by alloys. *J. Appl. Electrochem.* **21**, 967–972 (1991).
21. Chen, S., Huang, H., Liu, C. & Pan, Y. Technique for detecting sensitization in austenitic stainless steel. *Corrosion* **48**, 594–598 (1992).
22. Kang, J. & Frankel, G. Potentiostatic pulse testing for assessment of early coating failure. *Z. Phys. Chem.* **219**, 1519–1537 (2005).
23. Gao, J., Jiang, Y., Deng, B., Ge, Z. & Li, J. Determination of pitting initiation of duplex stainless steel using potentiostatic pulse technique. *Electrochim. Acta* **55**, 4837–4844 (2010).
24. Vignal, V. et al. Influence of the microstructure on the corrosion behaviour of low-carbon martensitic stainless steel after tempering treatment. *Corros. Sci.* **85**, 42–51 (2014).
25. Erazmus-Vignal, P., Vignal, V., Saedlou, S. & Krajcarz, F. Corrosion behaviour of sites containing (Cr, Fe)<sub>2</sub>N particles in thermally aged duplex stainless steel studied using capillary techniques, atomic force microscopy and potentiostatic pulse testing method. *Corros. Sci.* **99**, 194–204 (2015).
26. Vignal, V., Richoux, V., Suzon, E., Thiébaud, S. & Tabaleiv, K. The use of potentiostatic pulse testing to study the corrosion behavior of welded stainless steels in sodium chloride solution. *Mater. Des.* **88**, 186–195 (2015).
27. Frankel, G. S., Stockert, L., Hunkeler, F. & Boehni, H. Metastable pitting of stainless steel. *Corrosion* **43**, 429–436 (1987).
28. Chen, B. et al. Use of the potentiostatic pulse technique to study and influence pitting behavior of 317L stainless steel. *J. Electrochem. Soc.* **167**, 041509 (2020).
29. Hsieh, C.-C. & Wu, W. Overview of intermetallic sigma ( $\sigma$ ) phase precipitation in stainless steels. *ISRN Metall.* **2012**, 1–16 (2012).
30. Jang, A. Y. & Lee, H. W. Influence of sigma phase on pitting resistance depending on solidification mode in AISI316L weld metal. *Metall. Mater. Trans. A* **43**, 1736–1741 (2012).
31. Lippold, J. C. & Kotecki, D. J. *Welding Metallurgy and Weldability of Stainless Steels* (Wiley-VCH, 2005).
32. Villanueva, D. M. E., Junior, F. C. P., Plaut, R. L. & Padilha, A. F. Comparative study on sigma phase precipitation of three types of stainless steels: austenitic, superferritic and duplex. *Mater. Sci. Technol.* **22**, 1098–1104 (2006).
33. Padilha, A. F. & Rios, P. R. Decomposition of austenite in austenitic stainless steels. *ISIJ Int.* **42**, 325–327 (2002).
34. Ziętala, M. et al. The microstructure, mechanical properties and corrosion resistance of 316L stainless steel fabricated using laser engineered net shaping. *Mater. Sci. Eng. A* **677**, 1–10 (2016).
35. Guilherme, L. H., Benedetti, A. V., Fugivara, C. S., Magnabosco, R. & Oliveira, M. F. Effect of MAG welding transfer mode on sigma phase precipitation and corrosion performance of 316L stainless steel multi-pass welds. *J. Mater. Res. Technol.* **9**, 10537–10549 (2020).
36. Yongqiang, W., Hao, S., Na, L., Yanhao, X. & Hemin, J. Effect of sigma phase precipitation on the pitting corrosion mechanism of duplex stainless steels. *Int. J. Electrochem. Sci.* **13**, 9868–9887 (2018).
37. Eklund, G. S. Initiation of pitting at sulfide inclusions in stainless steel. *J. Electrochem. Soc.* **121**, 467 (1974).
38. Stewart, J. & Williams, D. E. The initiation of pitting corrosion on austenitic stainless steel: on the role and importance of sulphide inclusions. *Corros. Sci.* **33**, 457–474 (1992).
39. Ryan, M. P., Williams, D. E., Chater, R. J., Hutton, B. M. & McPhail, D. S. Why stainless steel corrodes. *Nature* **415**, 770–774 (2002).
40. Muto, I., Ito, D. & Hara, N. Microelectrochemical investigation on pit initiation at sulfide and oxide inclusions in type 304 stainless steel. *J. Electrochem. Soc.* **156**, C55 (2009).
41. Duret-Thual, C., Costa, D., Yang, W. P. & Marcus, P. The role of thiosulfates in the pitting corrosion of Fe-17Cr alloys in neutral chloride solution: electrochemical and XPS study. *Corros. Sci.* **39**, 913–933 (1997).
42. Ryan, M. P., Laycock, N. J., Isaacs, H. S. & Newman, R. C. Corrosion pits in thin films of stainless steel. *J. Electrochem. Soc.* **146**, 91–97 (1999).
43. Penot, C., Wharton, J., Addison, A., Wang, Y. & Lu, Q. Heat treatment effects on the corrosion performance of wire arc additively manufactured er316lsi stainless steel. *npj Mater. Degrad.* **7**, 48 (2023).
44. Wang, C., Zhu, P., Wang, F., Lu, Y. H. & Shoji, T. Anisotropy of microstructure and corrosion resistance of 316L stainless steel fabricated by wire and arc additive manufacturing. *Corros. Sci.* **206**, 110549 (2022).
45. Zhong, Y., Zheng, Z., Li, J. & Wang, C. Fabrication of 316L nuclear nozzles on the main pipeline with large curvature by CMT wire arc additive manufacturing and self-developed slicing algorithm. *Mater. Sci. Eng. A* **820**, 141539 (2021).
46. Long, J. et al. High-power wire arc additive manufacturing of stainless steel with active heat management. *Sci. Technol. Weld. Joining.* **27**, 256–264 (2022).
47. Lee, S. H. CMT-based wire arc additive manufacturing using 316L stainless steel: effect of heat accumulation on the multi-layer deposits. *Metals* **10**, 278 (2020).

## ACKNOWLEDGEMENTS

This work was made possible by the sponsorship and support of Lloyd's Register Foundation. Lloyd's Register Foundation helps to protect life and property by supporting engineering-related education, public engagement and the application of research. The work was enabled through, and undertaken at, the national Centre for Advanced Tribology at Southampton (nCATS), and the National Structural Integrity Research Centre (NSIRC), a postgraduate engineering facility for industry-led research into structural integrity established and managed by TWI through a network of both national and international Universities. The authors would also like to acknowledge the Lloyd's Register Industrial Mentor Mr Adam Saxty for his technical input. For the purpose of open access, the author has applied a CC BY public copyright licence to any Author Accepted Manuscript version arising from this submission.

## AUTHOR CONTRIBUTIONS

C.P.: conceptualization and methodology, original manuscript writing, experimental work, data interpretation. J.W.: conceptualization and methodology, data interpretation, manuscript review and editing. A.A.: manufacturing insight - WAAM wall deposition, specimens extraction and heat treatment. Y.W. and Q.L.: corrosion data interpretation, manuscript review and editing.

## COMPETING INTERESTS

The authors declare no competing interests.

## ADDITIONAL INFORMATION

**Supplementary information** The online version contains supplementary material available at <https://doi.org/10.1038/s41529-023-00408-8>.

**Correspondence** and requests for materials should be addressed to Corentin Penot.

**Reprints and permission information** is available at <http://www.nature.com/reprints>

**Publisher's note** Springer Nature remains neutral with regard to jurisdictional claims in published maps and institutional affiliations.



**Open Access** This article is licensed under a Creative Commons Attribution 4.0 International License, which permits use, sharing, adaptation, distribution and reproduction in any medium or format, as long as you give appropriate credit to the original author(s) and the source, provide a link to the Creative Commons license, and indicate if changes were made. The images or other third party material in this article are included in the article's Creative Commons license, unless indicated otherwise in a credit line to the material. If material is not included in the article's Creative Commons license and your intended use is not permitted by statutory regulation or exceeds the permitted use, you will need to obtain permission directly from the copyright holder. To view a copy of this license, visit <http://creativecommons.org/licenses/by/4.0/>.

© The Author(s) 2023